Superconductor
Science and
Technology

PURPOSE-LED
PUBLISHING™

PAPER • **OPEN ACCESS**

Highly crystalline superconducting TiN resonators grown on thermally reconstructed sapphire

To cite this article: Thomas J Smart *et al* 2026 *Supercond. Sci. Technol.* **39** 095021

View the article online for updates and enhancements.

You may also like

- Development of a microwave SQUID multiplexer for superconducting transition-edge sensor bolometer arrays
Zhifa Feng, Xianfeng Zhou, Min Li et al.
- Additional pinning induced by high growth rates in $YBa_2Cu_3O_7$ films containing nanorods
Ryoya Jindo, Yutaka Yoshida, Nao Ikemoto et al.
- Benchmarking reproducible low-loss wire-bond interconnects for superconducting quantum computing
Zilin Wang, Zihao Zhang, Yuzhe Xiong et al.

kiutra

Millikelvin characterization for superconducting devices

L-TYPE RAPID

- **< 4 hrs** sample loading and cooldown to base
- **50 mK** base temperature
- **30 min** warm up and sample exchange

Find out more →



This content was downloaded from IP address 134.130.185.47 on 06/10/2026 at 14:48

Superconductor Science and Technology

Check for updates

OPEN ACCESS

RECEIVED
8 July 2026

REVISED
26 August 2026

ACCEPTED FOR PUBLICATION
17 September 2026

PUBLISHED
28 September 2026

Original content from this work may be used under the terms of the Creative Commons Attribution 4.0 licence.

Any further distribution of this work must maintain attribution to the author(s) and the title of the work, journal citation and DOI.

PAPER

Highly crystalline superconducting TiN resonators grown on thermally reconstructed sapphire

Thomas J Smart[1], Marc Neis[2,3], Janine Lorenz[4,5], Marcello P Guardascione[2,3], Roudy Hanna[1,2,3], Michael Schleenvoigt[1], Yuan Gao[2,3], Joscha Domnick[1], Benjamin Bennemann[6], Abdur Rehman Jalil[6,7], Jin Hee Bae[1], Harsh Bhardwaj[2,3], F Stefan Tautz[4,5], Felix Lüpke[4,8], Detlev Grützmacher[1], Rami Barends[2,3], Pavel A Bushev[2] and Peter Schüffelgen[1,*]

[1] Peter Grünberg Institute (PGI-9), Forschungszentrum Jülich and JARA Jülich-Aachen Research Alliance, 52425 Jülich, Germany
[2] Institute for Functional Quantum Systems (PGI-13), Forschungszentrum Jülich, 52425 Jülich, Germany
[3] RWTH Aachen University, 52074 Aachen, Germany
[4] Peter Grünberg Institute (PGI-3, Forschungszentrum Jülich and JARA Jagalich-Aachen Research Alliance, Jülich 52064, Germany
[5] Institute of Experimental Physics IV A, RWTH Aachen University, 52074 Aachen, Germany
[6] Peter Grünberg Institute (PGI-10), Forschungszentrum Jülich and JARA Jülich-Aachen Research Alliance, 52425 Jülich, Germany
[7] Institute for Experimental Physics III, University of Würzburg, 97074 Würzburg, Germany
[8] Institute of Physics II, University of Cologne, 50937 Cologne, Germany
* Author to whom any correspondence should be addressed.

E-mail: p.schueffelgen@fz-juelich.de

Keywords: titanium nitride, resonators, molecular beam epitaxy, sapphire

Abstract

High-quality crystalline growth of a thin film on sapphire requires sufficient substrate preparation, often achieved via aggressive chemical cleaning. Direct thermal reconstruction of the sapphire substrate via a CO_2 laser beam may provide an alternative method to prepare the substrate for epitaxy without the use of any chemical processing. In this work, we demonstrate that the thermal annealing of sapphire into its $(\sqrt{31} \times \sqrt{31})\, R\pm 9°$ reconstruction is a valid alternative preparation technique for sapphire substrates. TiN films grown via plasma-assisted molecular beam epitaxy upon these substrates exhibit greater crystallinity than those grown on chemically-cleaned sapphire substrates. Superconducting resonators fabricated from these films exhibit similar performance, with many possessing internal quality factors at single photon levels greater than 10^6 for both substrate preparation methods.

1. Introduction

While Nb-based technologies have a long history in superconducting electronics [1], Al/AlO_x has become a widely adopted material system for superconducting quantum circuits [2, 3]. Alongside these established platforms, alternative superconducting materials have been investigated for decades with the aim of improving device performance and expanding fabrication capabilities [4–6]. Superconducting transition metal nitrides (TMNs) have attracted significant attention because of their desirable properties, such as a large superconducting gap, high critical temperature, T_c, and resistance to oxidation and chemical etching [7, 8].

Titanium Nitride (TiN) is a metallic compound that is readily used within the semiconductor industry due to its desirable properties, such as: high electrical conductivity, compatibility with existing CMOS technology and chemical stability [9, 10]. Despite its lower T_c and superconducting gap size, TiN offers a comparatively simple phase-stability landscape for high-temperature epitaxial growth, compared to other popular superconducting TMNs, like the Nb-N system [11, 12]. In recent years, TiN has been shown to be a promising material for passive superconducting components, with the internal quality factors (Q_i) of prior superconducting co-planar waveguide (CPW) resonators, exceeding 10^6 at single photon levels for films grown on silicon and sapphire substrates [13–16]. Commonly reported methods for the chemical cleaning of sapphire substrates include organic solvent cleaning, typically using acetone and

© 2026 The Author(s). Published by IOP Publishing Ltd

isopropanol, as well as more aggressive treatments using Piranha solution or hydrofluoric acid (HF) to remove surface contaminants and obtain a clean substrate surface [17].

An alternative substrate preparation method is presented through the thermal reconstruction of the surface of the substrate [18]. In the case of sapphire substrates, *in-situ* direct heating by a CO_2 laser substrate heater, such as those available with thermal laser epitaxy (TLE) chambers, provides a rapid method to thermally prepare the substrate for further epitaxy. Crucially, this rapid thermal preparation of the substrate is performed without any aggressive $ex-situ$ chemical preparation [19, 20]. *C*-plane sapphire substrates that have been reconstructed into the characteristic $(\sqrt{31}\times\sqrt{31})$ $R\pm9°$ (R31) reconstruction have been shown to enable the high-quality crystalline growth of various materials with pristine interface quality and exemplary electronic properties [19, 21–24]. Given this platform, an intriguing opportunity is presented to observe if thermal reconstruction of the sapphire substrate impacts the performance of a simple superconducting device, such as a CPW resonator, that has been epitaxially grown upon the substrate. This can then be compared to a sister device grown and fabricated on sapphire substrates that have been prepared with aggressive chemicals.

Within this work, we epitaxially grow highly crystalline TiN (111) films on both chemically-cleaned *c*-plane sapphire and thermally reconstructed R31 sapphire via plasma-assisted molecular beam epitaxy (MBE). It was observed that TiN films grown on reconstructed sapphire exhibit a greater degree of crystallinity compared to those grown on sapphire prepared via aggressive acids. By etching the films using resist-based lithography, we manufacture superconducting CPW resonators from these films. For both preparation methods, we observe Q_i values exceeding 10^6 at single photon values, indicating that thermal reconstruction provides a rapid and simple alternative to substrate preparation via aggressive acids, without significantly affecting superconducting properties of the films nor the performance of a corresponding superconducting device.

2. Methods

2.1. Growth

Pre-diced 10 × 10 mm^2 pieces of *c*-plane sapphire (α-Al_2O_3) supplied by CrysTec GmbH were used as the substrate during this work. Before any further processing of the substrates in a cleanroom environment, all substrates were first cleaned with an acetone and isopropanol (IPA) bath of 5 min each with sonication, before further chemical or thermal treatment to avoid equipment contamination. A selection of these substrates were then chemically processed further in a Piranha solution mix of 2:1 H_2SO_4:H_2O_2 for 10 min, followed by a dip in a 1% solution of HF for 1 min. A final cleaning step of a 10 min dip in deionized water followed by a 2 min dip in isopropanol was performed to remove any volatile products and ensure a clean surface. These chemically-processed Al_2O_3 substrates were then loaded into an ultra-high vacuum (UHV) preparation chamber, where they were baked at 900 ° C for 45 min to prepare an epi-ready surface without forming a surface reconstruction [25]. After baking, these substrates were loaded into the MBE chamber for deposition. Sapphire substrates cleaned in this manner will be hereon referred to as 'Bare' sapphire or B-Al_2O_3.

Another portion of the acetone/IPA cleaned substrates were prepared thermally by loading them into a TLE system, which operates at UHV conditions with a chamber pressure $p\sim1\times10^{-9}$ mbar during laser irradiation [26–28]. This system is equipped with a CO_2 laser substrate heater with a laser beam diameter of 5 cm, capable of directly heating the Al_2O_3 substrates to extremely high temperatures [20, 23, 29]. This method provides a far greater range of substrate temperatures without the risk of contamination caused by indirect heating via wire heaters or tube furnaces [18]. Under these conditions, the surface of the Al_2O_3 substrates reforms into the R31 reconstruction described previously. The Al_2O_3 substrates were held at 1700 °C for 200 s, forming a terraced structure with a step height of ∼0.4 nm, corresponding to two atomic layers of the Al_2O_3 unit cell as previously described in prior literature [20]. The presence of a R31 surface reconstruction was verified via reflection high-energy electron diffraction (RHEED) imaging performed after heating, in which a clear double-step R31 reconstruction is observed. These images are shown within appendix A.

The change in the surface morphology during surface reconstruction compared to chemically cleaned Al_2O_3 is shown in figures 1(a) and (b), respectively. Parallel to each terrace on the reconstructed sapphire, the root-mean-square (RMS) roughness is noticeably lower compared to the bare sapphire substrate. The flat and well-ordered surface morphology provides a favorable platform for epitaxy with atomically sharp interfaces compared to unreconstructed Al_2O_3, which recent literature has shown does not provide a uniform and smooth (1 × 1) surface [30]. The use of reconstructed R31-Al_2O_3 within

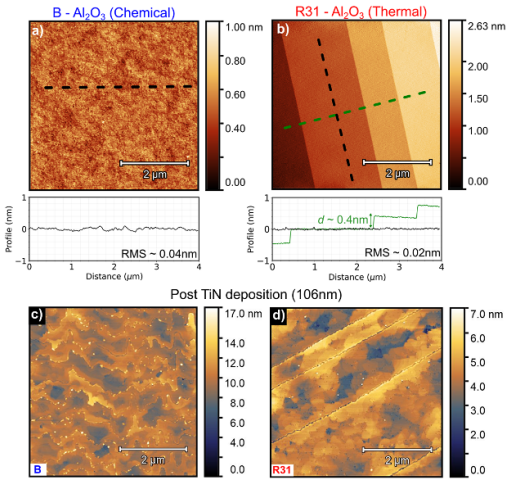


Figure 1. (a) and (b) AFM topographs of *c*-plane sapphire substrates, after chemical cleaning with Piranha solution and 1% HF (B-Al_2O_3) and after thermal annealing to form the $(\sqrt{31} \times \sqrt{31})$ $R\pm9°$ reconstruction at $T_{sub} = 1700\,°C$ for 200 s (R31-Al_2O_3). Height profiles along indicated paths are shown underneath each AFM topograph with the calculated RMS roughness noted for each substrate. (c) and (d) AFM topographs of $d = 106$ nm TiN films grown at 1150 °C.

physical vapor deposition and epitaxy promotes the growth of highly crystalline thin films with exemplary crystal properties, as previously demonstrated for various material systems [19, 21, 22, 24]. As confirmed by the RHEED images in appendix A and in prior literature, once the R31 reconstruction has formed, it remains stable in air, even after months in atmospheric conditions [20]. Consequently, *ex − situ* transfer of the reconstructed sapphire between the TLE chamber and any separate growth chamber did not effect the quality of substrate, provided that any volatile products like water vapor were removed prior to epitaxy [20]. Sapphire substrates prepared in this manner will be henceforth referred to as R31-Al_2O_3.

A selection of B-Al_2O_3 and R31-Al_2O_3 substrates were then simultaneously loaded into a MBE chamber, where they were first baked at 200 °C for 45 min to remove any lingering water vapor or other adsorbents. Prior to growth, the chamber operated under UHV conditions with $p \sim 1 \times 10^{-10}$ mbar. During growth within the MBE chamber, an atomic nitrogen (N) atmosphere was provided by a Radio Frequency (RF) plasma source with an RF power of 400 W and a N flow rate of 1.25 sccm, providing a chamber pressure of 1.5×10^{-4} mbar during growth. Titanium (Ti) was provided via an e-beam evaporator held at a partial pressure of 1×10^{-8} mbar, resulting in a TiN growth rate of ~ 0.4Å s^{-1}. Films with a thickness $d = 106$ nm of TiN were grown at 1150 °C. To ensure the stoichiometry of the deposited TiN is as close to the desired 1:1 atomic ratio of Ti:N as possible, the deposited film was held at 1100 °C for an hour within the atomic N atmosphere after growth was complete. This allowed for any volatile materials incorporated during growth to leave the TiN film whilst fully nitriding the remaining sample. The sample was then cooled back down to room temperature over the period of half an hour within the atomic N atmosphere. The presence of this atmosphere during cool down was designed to reduce the diffusion of N out of the TiN at high temperatures, which may negatively impact the superconducting properties of the grown TiN film [12]. A second set of TiN films with $d = 17$ nm were also grown on both R31-Al_2O_3 and B-Al_2O_3, under the same growth parameters described previously for imaging via Transmission Electron Microscopy (TEM). All other measurements were performed on the $d = 106$ nm TiN films.

2.2. Design and fabrication of resonators

Once growth was completed, the $d = 106$ nm TiN films were fabricated into $\lambda/4$ CPW resonators using a standard optical resist lithography process and dry etching. The samples were spin-coated with ECI-3012 (positive) photo-resist, soft baked at 90 ° C for 1 min and then patterned using direct laser writing via a Maskless Aligner device with a dose of 130 mJ cm^{-2}. The samples were then post-exposure baked at 110 °C for 1 min before developing the exposed resist via a 65 s dip in AZ-326 metal-ion free solution. The TiN films were then patterned via reactive ion etching using SF_6 gas with a flow rate of 30 sccm, an RF power of 25 W and an ICP power of 100 W. Once the samples had been etched, the remaining resist was removed with acetone and isopropanol dips of 10 min each. A drawing of the $\lambda/4$ CPW resonator design used in this work is given in figure 2(a).

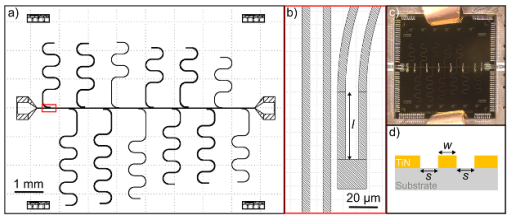


Figure 2. (a) Drawing of the $\lambda/4$ CPW resonator design used in this work. The four rectangular structures, each placed at the corners of each chip are four-point probe structures to measure the superconducting transition as a function of temperature (see appendix C). (b) Zoom in of resonator design showing the coupling between the central feedline and a resonator, with the coupler length, $l = 50\,\mu$m indicated. This value remained fixed for all resonators. (c) Photograph of 10×10 mm fabricated TiN resonator chip after bonding. (d) Cross-sectional diagram of CPW resonator, where the width of the central conductor, w and the gap size, s are indicated.

The structured CPW resonators were designed to have their resonance frequencies lie within the range of 4–8 GHz, consisting of a range of different structure sizes and coupling to a central readout line. For all resonators, the coupler length, l, as shown in figure 2(b), was fixed at 50 μm. The central conductor width, w and the gap size, s between the central conductor and the remaining TiN film was varied for each resonator. A full list of resonator parameters is given in appendix E.

2.3. Cryogenic measurement setup

The electronic properties of the material were probed in a BlueFors SD cryogenic dilution refrigerator, which cooled the samples down to ~20 mK. Using the build-in heaters the setup can be used at a range of temperatures to measure the resistance via four-point probe structures determining DC properties such as resistivity, ρ and T_c. Additionally, the cryogenic experiment was used to measure the electronic properties of any device at frequencies ranging from 3.5 GHz to 8.5 GHz. These chips were connected to custom made PCBs via Aluminum wire-bonding, which have SMA connectors for readout. A Keysight VNA (N5222B), in series with a total of 60 dB of attenuation on the various temperature stages, probed the S-parameters of the samples.

3. Results

3.1. Growth and film quality

The TiN films grown on reconstructed (R31-Al_2O_3) and bare sapphire (B-Al_2O_3) were analyzed with a variety of crystallography and imaging techniques. Firstly, the TiN films grown on R31-Al_2O_3 and B-Al_2O_3 have visually different morphologies. As shown in the Atomic Force Microscopy (AFM) micrographs in figures 1(c) and (d), TiN grown on R31-Al_2O_3 demonstrates a smoother surface morphology with micron-scale grains that are aligned with the underlying terrace structure of R31-Al_2O_3. For both substrate preparation methods, the TiN films exhibit epitaxial growth with a face-centered cubic structure and (111) surface orientation. As shown in figure 3(a), both films exhibit sharp and intense TiN (111) peaks. The fixed azimuthal relationship between the TiN (111) and Al_2O_3 poles is preserved for both films on R31-Al_2O_3 and B-Al_2O_3, indicating the same TiN/Al_2O_3 epitaxial registry in both films. Pole figures, shown with appendix B, reveal a sixfold TiN pole distribution that is consistent with two 60°-related in-plane rotational variants of TiN (111).

The quality of the TiN/Al_2O_3 interface was examined under cross-sectional TEM on two sister TiN samples with $d = 17$ nm. Owing to the large lattice mismatch between TiN(111) and c-plane Al_2O_3 of approximately 8.5%, epitaxial strain is relieved within the first few atomic layers due to the formation of interfacial misfit dislocations [31]. This results in the interface structure between TiN(111) and c-plane Al_2O_3 being fixed in the initial stages of growth [32]. Under identical deposition conditions, cross-sectional TEM performed on a $d = 17$ nm TiN film is therefore expected to be representative of the TiN/Al_2O_3 interface within thicker TiN films, although microstructural features within the film itself that evolve with film thickness, such as threading defects and grain morphology, may differ.

No significant visual evidence of intermixing between the TiN and R31-Al_2O_3 substrate was observed for either sample. There is some indication of a smoother interface between the TiN and R31-Al_2O_3, but both substrates exhibit a low surface roughness along the imaged crystal axis. This reduced roughness of R31-Al_2O_3 is consistent with the AFM measurements performed in figure 1 and supports the reduced

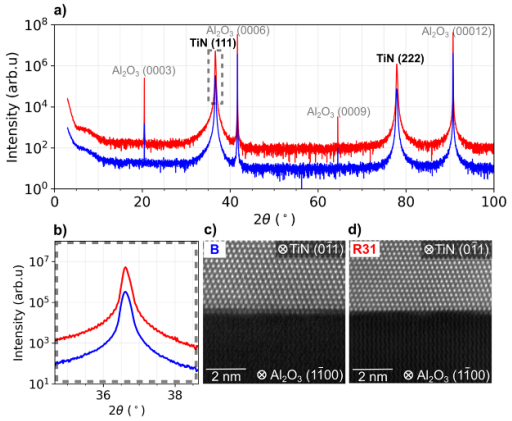


Figure 3. (a) Comparison of XRD spectra for $d = 106$ nm TiN films grown on reconstructed (R31-Al_2O_3—Red) and bare sapphire (B-Al_2O_3—Blue), where the relevant features have been indicated. The R31-Al_2O_3 curve has been vertically displaced by a factor of 10 for clarity. (b) Zoom-in on the TiN (111) peak from the XRD spectra. (c) and (d) Transmission Electron Microscopy (TEM) images of the TiN/Al_2O_3 interface of $d = 17$ nm thick TiN films for B-Al_2O_3 and R31-Al_2O_3 respectively. The interface appears sharper for R31-Al_2O_3 compared to B-Al_2O_3.

surface roughness of each terrace in the $(\sqrt{31} \times \sqrt{31})$ $R\pm9°$ reconstruction relative to its chemically-cleaned counterpart [20, 25].

A smoother R31-Al_2O_3 surface would serve as a favorable platform for greater crystalline coherence, due to its greater crystal order and lower surface roughness [30]. This is supported by rocking curve measurements around the TiN(111) peak for both $d = 106$ nm films, wherein the rocking curve for the TiN sample grown on R31-Al_2O_3 is noticeably more intense and sharper than the corresponding curve of TiN on B-Al_2O_3. When both curves are fit to a pseudo–Voigt dependence, shown as dotted lines in figure 4(a), the extracted full-width-half-maximum (FWHM) values for the TiN films on R31-Al_2O_3 and B-Al_2O_3 are 0.048° and 0.098° respectively.

From XRD measurements, Reciprocal Space Maps (RSMs) were extracted to elucidate how the distribution of in-plane ($a_{\parallel}$) and out-of-plane ($a_{\perp}$) lattice constants of the TiN films are effected by the different substrate preparation methods. Examining the off-axis (402) reflections of the TiN films allows for information regarding $a_{\parallel}$ and $a_{\perp}$ to be directly extracted. In figure 4(b), the corresponding RSMs from the TiN(402) reflection are overlaid, where only intensity values greater than half of the maximum intensity are plotted. For both substrates, $a_{\parallel}$ and $a_{\perp}$ are very similar in value, as expected for a cubic crystal structure. For R31-Al_2O_3, The TiN film possesses $a_{\parallel} = (4.245 \pm 0.003)$ Å and $a_{\perp} = (4.242 \pm 0.003)$ Å. For TiN grown on B-Al_2O_3, the film exhibits $a_{\parallel} = (4.244 \pm 0.007)$ Å and $a_{\perp} = (4.245 \pm 0.005)$ Å.

The extracted lattice constants correspond to in-plane strains of $\epsilon_{\parallel} = (0.021 \pm 0.064)\%$ and $\epsilon_{\parallel} = (0.002 \pm 0.165)\%$ for TiN on R31- and B-Al_2O_3 respectively, relative to bulk TiN (a = 4.244 Å) [33, 34]. The corresponding out-of-plane strains are $\epsilon_{\perp} = (-0.048 \pm 0.072)\%$ and $\epsilon_{\perp} = (0.024 \pm 0.118)\%$.

Both in-plane and out-of-plane strain values are relatively small, suggesting that the film is largely relaxed. The contour shapes shown in figure 4(b) further support these interpretations; the elongated distribution for B-Al_2O_3 lies along a single primary axis in the $a_{\parallel}$—$a_{\perp}$ plane, reflecting correlated fluctuations between in-plane and out-of-plane lattice constants. This behavior is characteristic of microstrain broadening and mosaic disorder, where minor local lattice tilts and distortions contribute to the spread of values [35, 36]. In contrast, the nearly circular contour for R31-Al_2O_3 indicates an isotropic distribution of lattice constants, consistent with a more uniform strain state and reduced defect density. The overall weaker intensity and larger spread for B-Al_2O_3 suggest a smaller coherent scattering volume, likely arising from higher dislocation density or reduced grain size, whereas the sharper, more intense distribution for R31-Al_2O_3 reflects improved crystalline coherence. When taken together, these results point to R31-Al_2O_3 providing a more favorable template for crystalline TiN growth, enabling reduced mosaicity and with more homogeneous strain relaxation compared to B-Al_2O_3.

Both TiN films were measured to turn superconducting with $T_c = 5.08$ K and 5.11 K for B-Al_2O_3 and R31-Al_2O_3 respectively. Via the use of fabricated four-point probe structures, ρ of each film was measured at room temperature and at temperatures close to T_c. From these measurements, the Residual Resistance Ratio value for each film was calculated. These were found to be broadly similar at 2.64 and 2.62 for B-Al_2O_3 and R31-Al_2O_3 respectively, supporting the comparable level of film quality between both samples observed in figure 3.

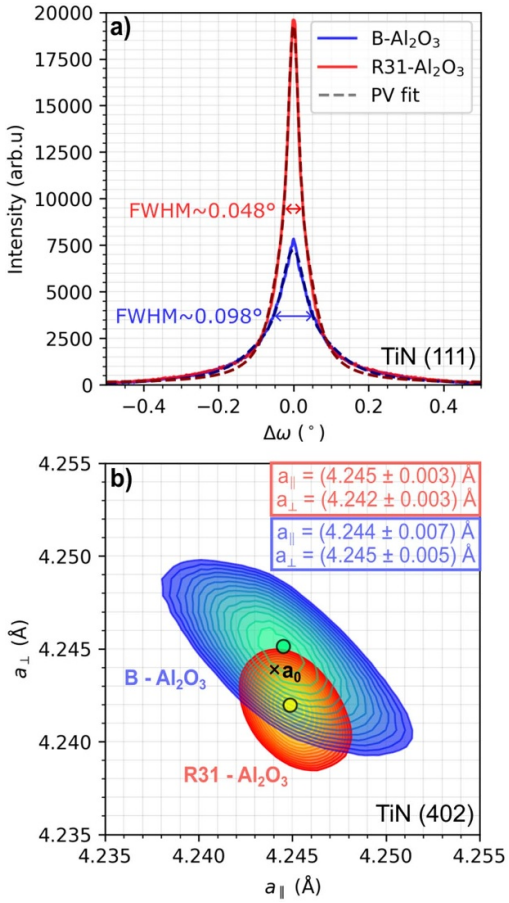


Figure 4. (a) TiN (111) rocking curves for $d = 106$ nm grown on R31-Al_2O_3 and B-Al_2O_3. Both curves have been fit to a Pseudo–Voigt (PV) distribution (shown as dotted lines) to extract the FWHM values of 0.048° and 0.098° respectively. (b) RSM plots of the off-axis TiN (402) peak showing the distribution of in-plane ($a_{\parallel}$) and out-of-plane ($a_{\perp}$) lattice constants for each film. Only intensity values greater than 50% of the maximum value have been plotted for clarity. The literature value of the TiN lattice constants, (a_0) is indicated by a black cross whilst the peak intensity for each distribution is indicated by a colored dot. The average value for $a_{\parallel}$ and $a_{\perp}$ for each film is also indicated.

Whilst it is evident that TiN grown at high temperatures on R31-Al_2O_3 exhibits greater crystallinity, it may not definitively translate to the superconducting properties, particularly since both can be considered to be disordered superconductors [37, 38]. To probe if the observed differences in film crystallinity translate to changes in the superconducting properties, we perform scanning tunneling microscopy/spectroscopy (STM/S) measurements. STS allows to determine the size and uniformity of the superconducting gap across the sample surface. Although STS measurements cannot directly probe the substrate-film interface, it can detect changes in the film properties at the sample surface, which arise from differences at the substrate–film interface, similar to the observed changes in surface morphology (figures 1 and D4).

Prior to STM/S measurements the samples were degassed *in-situ* at 280 °C for 20 min to remove surface adsorbates. Cleaning via ion bombardment was avoided to minimize the risk of surface defect formation. Subsequently, the samples were transferred into a Createc scanning tunneling microscope and cooled down to 1.2 K. All STM/S experiments were performed with an Ag-coated PtIr tip.

STM topographs are shown in appendix D and are in broad agreement with the AFM data displayed in figures 1(c) and (d). Figure 5(a) shows differential conductance spectra measured across representative areas of the B-Al_2O_3 and R31-Al_2O_3 sample respectively. A linear background was subtracted from each spectrum. From the STS data, three main conclusions can be drawn. Firstly, both the gap width and coherence peak height were not uniform along the measured lines. Clear variations in both parameters were observed on a length scale of 20–50 nm. This observation is consistent with previous STS measurements on homogeneously disordered superconducting thin films [37, 38]. Secondly, in-gap states were observed, particularly on the R31-Al_2O_3 sample. Such sub-gap spectral weight has also been observed in STM measurements of TiN and may arise from local variations in tunneling conditions, surface disorder, or Andreev contributions at highly transparent tip–sample contacts [39]. Thirdly, some spectra showed

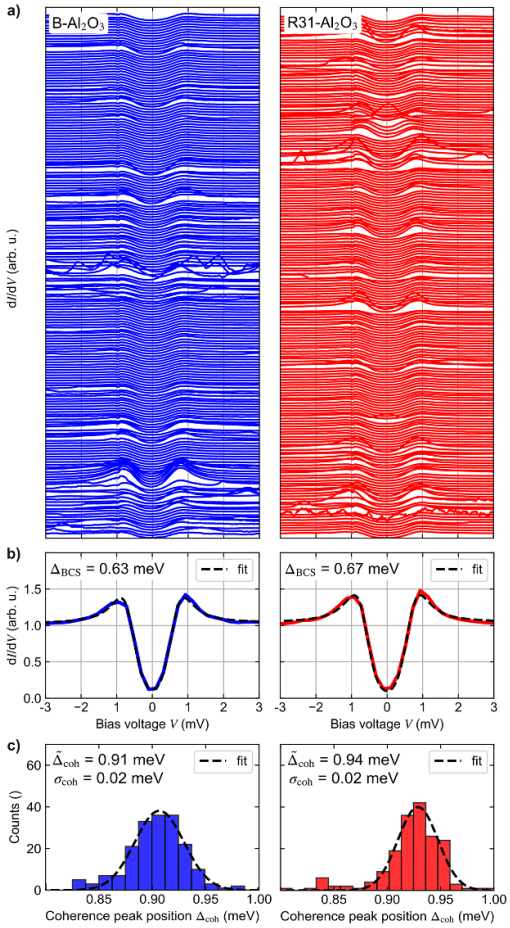


Figure 5. (a) Waterfall plot of 200 differential tunneling conductance spectra recorded along a 424 nm line across a representative area of the surface of each TiN film with $d = 106$ nm grown on B-Al_2O_3 and R31-Al_2O_3 (successive spectra are taken every 2.1 nm, and are offset vertically). (b) Average of the 200 spectra shown in (a) including BCS fits which yield order parameters of $\Delta_{BCS} = 0.63$ and 0.67 meV as well as effective temperatures of $T_{tip} = 1.90$ and 1.91 K for the samples B-Al_2O_3 and R31-Al_2O_3 respectively. (c) Distribution of the energy at which the coherence peak maxima occur Δ_{coh} in the spectra shown in panel (a) The mean values and standard deviations of the distributions are determined from the shown Gaussian fits and indicated as insets. Tunneling spectra were recorded at an STM temperature of 1.2 K with a set point current of 1 nA and a lock-in amplitude of 0.08 mVpp at a modulation frequency of 819 Hz.

unstable tunneling, which results in a noisy signal and little to no superconducting gap. We attribute this to possible surface contamination caused by exposure of the films to air.

In figure 5(b), the average differential conductance spectra of the data shown in figure 5(a) are plotted together with the corresponding fits of the Bardeen–Cooper–Schrieffer (BCS) density of states (DOS) [40]:

$$n_{BCS}(E) = n_0 \,\mathrm{Re}\left[\frac{|E|}{\sqrt{E^2 - \Delta_{BCS}^2}}\right], \tag{1}$$

where n_0 is the normal state DOS, E is the energy and Δ_{BCS} is the superconducting pairing gap. In our experiment, we assumed a flat tip DOS and a constant tunneling matrix element, which allows us to use a simplified relation between the measured $\mathrm{d}I/\mathrm{d}V$ and n_{BCS}:

$$\mathrm{d}I/\mathrm{d}V \propto \int_{-\infty}^{\infty} \mathrm{d}E \left[\frac{\mathrm{d}}{\mathrm{d}V} f_{tip}(E)\right] n_{BCS}(E + eV), \tag{2}$$

where e is the elementary charge and $f_{tip}(E) = 1/[1 + \exp(E/k_B T_{tip})]$, the Fermi–Dirac distribution function of the tunneling tip. From the fits in figure 5(b), pairing gaps of $\Delta_{BCS} = (0.63 \pm 0.01)$ and (0.67 ± 0.01)MeV were obtained for the B-Al_2O_3 and R31-Al_2O_3 samples respectively. Note that, while the majority of the spectra from figure 5(a) are well described by the BCS scenario, the BCS gaps resulting from figure 5(b) are averaged values that also include spectra with in-gap states. Such states broaden the averaged $\mathrm{d}I/\mathrm{d}V$ spectra, which can explain the increased effective temperatures of $T_{tip} \approx 1.90$ K

resulting from the fits. To clarify this issue, we plot the energy distributions of the coherence peak maxima in figure 5(c). The histograms emphasize that there are a few outliers corresponding to spectra with in-gap states, while the majority of spectra has coherence peaks centered around the mean values of $\tilde{\Delta}_{\mathrm{coh}} = 0.91\,\mathrm{MeV}$ and 0.94 MeV for the B-Al_2O_3 and R31-Al_2O_3 sample respectively. By fitting these histograms to a Gaussian function:

$$g(\Delta) \propto \exp\left(-\frac{1}{2}\frac{\left(\Delta_{\mathrm{coh}} - \tilde{\Delta}_{\mathrm{coh}}\right)^2}{\sigma_{\mathrm{coh}}^2}\right). \tag{3}$$

We further extract the width of the coherence peak distributions variations as $\sigma_{\mathrm{coh}} = 0.02\,\mathrm{MeV}$ for both samples. The small differences in the coherence peak positions are within observed variations measured across different locations on the samples.

From the fitted order parameters, we calculate the BCS gap ratio $2\Delta_{\mathrm{BCS}}(0)/k_{\mathrm{B}}T_{\mathrm{c}}$. For sample B-$Al_2O_3$, we obtain 2.88, and for sample R31-Al_2O_3, 3.04. Both values are below the weak-coupling BCS value of 3.53. Nevertheless, we believe that our samples are well described by the BCS scenario, as this discrepancy can be explained by spatial inhomogeneities in our films: Fits of the averaged tunneling spectra in figure 5(b) reflect the average order parameter across the surface. In contrast, T_{c} determined from transport measurements corresponds more closely to the temperature below which a supercurrent can flow through interconnected regions with the largest order parameter. Based on the variations of the coherence peak positions shown in figure 5(c), we expect the variations in the order parameter throughout the film to be on the order of $\sim$10 %. Within this variation, the gap ratio approximately reaches the expected BCS value of 3.53. Remaining discrepancies may stem from STS being more sensitive to defects located at the film surface, especially in the film's native oxide layer. Such defects can locally weaken superconductivity, and therefore reduce the order parameter of the tunneling spectra (see figure 5(a)) and thus the BCS gap ratio.

From these results, we conclude from the STS measurements that the pairing gap of the TiN films grown on both B-Al_2O_3 and R31-Al_2O_3 are comparable. No significant influence of the thermal reconstruction of R31-Al_2O_3 on the pairing gap of TiN was observed, resulting in TiN films grown on both B-Al_2O_3 and R31-Al_2O_3 possessing similar superconducting properties.

3.2. TiN CPW resonators

Finally, superconducting CPW resonators were fabricated from both TiN films in order to assess if the differences observed in crystalline quality with similar superconducting properties can effect the properties of said resonators.

A full list of the parameters of all resonators on each chip are given in appendix E. From the raw Q_{i} data for all resonators on each chip, a median $Q_t extrmi$ as a function of photon number, $\langle n \rangle$ was calculated and is indicated in figure 6(a), with a confidence interval equal to one standard deviation as a measure of device-to-device performance for resonators on a given chip. The raw Q_{i} data for all resonators on each chip are shown in appendix E, with the confidence interval overlaid. Figure 6(b) shows the distribution of Q_{i} values at $\langle n \rangle \sim 1$ across all resonators, for which single-photon data was available, on each chip. For both chips, a majority of resonators had Q_{i} values exceeding 10^6, similar to what has been observed in prior literature on TiN resonators [13, 15, 41]. Median Q_{i} values of the TiN resonators at single photon values were calculated at 1.33×10^6 and 1.13×10^6 for B-Al_2O_3 and R31-Al_2O_3 respectively. For each chip, the confidence interval at single photon levels spanned from $1.19 \times 10^6 - 1.73 \times 10^6$ and $0.35 \times 10^6 - 1.31 \times 10^6$ for B-Al_2O_3 and R31-Al_2O_3 respectively. All measured resonators exhibited a characteristic dip in its corresponding, frequency-dependent transmission function S_{21}, and the expected circular profile in complex space, examples of which on each chip are shown in appendix E at single photon levels with corresponding fits [42, 43]. The corresponding parameters for each resonator on both B-Al_2O_3 and R31-Al_2O_3 are also given in appendix E. For both chips, several resonators possessed Q_{i} values exceeding 10^7 at high photon numbers, matching values measured in similar TiN resonators in prior literature [15, 41, 44].

4. Discussion

Both TiN films grown on R31-Al_2O_3 and B-Al_2O_3 exhibit epitaxial growth of the TiN (111) phase, as evidenced by the XRD spectra shown in figure 3. Compared to the TiN film on B-Al_2O_3, the film grown on R31-Al_2O_3 demonstrates superior crystalline order and a reduced mosaic spread of TiN grains. This

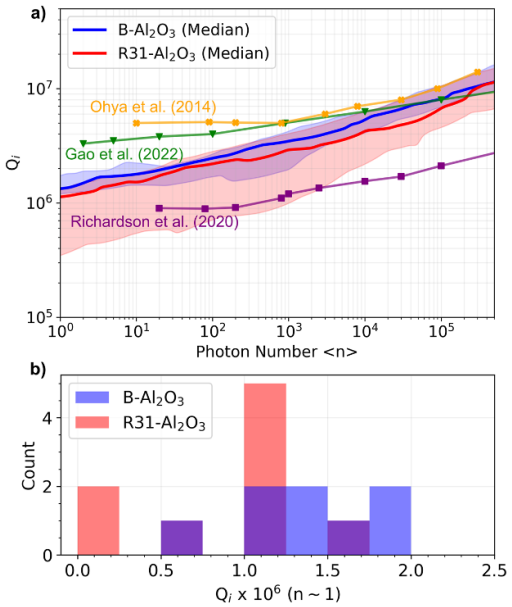


Figure 6. (a) Median internal quality factor (Q_i) of TiN CPW resonators fabricated from $d = 106$ nm TiN films grown on R31-Al_2O_3 and B-Al_2O_3 respectively. The median value was only calculated from resonators where single-photon data was available. A confidence interval of one standard deviation for Q_i values across all resonators on each chip is also indicated by the corresponding colored envelope. Selected Q_i values from literature are also shown, with the values obtained here being similar to those achieved previously [13, 15, 41]. (b) Histogram of single photon Q_i values for all resonators on each chip.

suggests that the atomically ordered surface of R31-Al_2O_3 facilitates coherent rotational alignment of the TiN film, thereby minimizing grain misorientation. Furthermore, the atomically-smooth terrace surface of R31-Al_2O_3 promotes single-domain epitaxy, enabling the formation of large grains and step-flow growth. This is supported by the replication of the underlying terrace structure of the R31-Al_2O_3 substrate in the deposited TiN film [20, 24, 45]. The T_c values of these TiN films were measured at 5.11 K and 5.08 K on R31-Al_2O_3 and B-Al_2O_3, respectively. These values fall below the state-of-the-art value of $T_c \sim 5.7$ K recorded for thin films grown via magnetron sputtering or TLE [24, 46]. Firstly, the TiN films presented in this work were deposited at 1150°C, a temperature at which the rate of nitrogen diffusion out of the deposited film becomes significant [47]. This stands in contrast to the growth of TiN via magnetron sputtering which is typically performed at significantly lower substrate temperatures or from stoichiometric targets [15, 41, 46]. High temperature deposition would then result in small changes in the stoichiometry of the TiN, potentially via the formation of N vacancies, which would then reduce the T_c of the film compared to bulk values. In order to minimize the potential presence of N vacancies and potentially improve the stoichiometry of TiN films grown at high substrate temperatures, the use of an Ammonia (NH_3) atmosphere during growth may be desirable, as demonstrated in prior literature demonstrating the growth of highly crystalline superconducting TMNs with state-of-the-art properties [24].

Despite the clear advantages in crystal quality when growing TiN on R31-Al_2O_3, TiN resonators on R31-Al_2O_3 and B-Al_2O_3 exhibit similarly high Q_i values, with low-power Q_i values greater than 10^6 for many resonators. As shown in figure 6, this performance is consistent with other TiN resonators from literature, including TiN films grown via MBE [13] or those grown via conventional sputtering methods [15, 41]. However, we caution that directly comparing our work with prior literature may be misleading due to differing resonator geometries, growth mechanisms and choices in substrate material, all of which impact the extracted values of Q_i. In addition, we note that some prior literature may only report the measured Q_i values from a small number of resonators, whereas the median Q_i values presented in this work are calculated across all resonators on each chip.

A greater variation in resonator performance is observed for TiN resonators grown on R31-Al_2O_3 compared to B-Al_2O_3. However, the larger spread of low-power Q_i values observed for resonators on R31-Al_2O_3 does not appear to correlate directly with the improved crystalline quality of the TiN film. In particular, the lowest-Q_i devices on the R31 chip occur among resonators with the narrowest CPW geometry ($w = 3\,\mu$m, $s = 2\,\mu$m), for which the electric-field participation of the metal–vacuum and substrate–vacuum interfaces is enhanced [48]. At single-photon powers, losses in TiN CPW resonators are known to be strongly influenced by TLS associated with processed surfaces and interfaces, and recent

studies indicate that fabrication conditions and interfacial oxide chemistry can affect microwave loss more strongly than the crystalline orientation of the TiN film itself [48–50]. Consequently, local variations introduced during lithography, dry etching, resist removal or subsequent surface oxidation could produce appreciable device-to-device variation without being reflected in the XRD, transport or STS properties of the film. With the present number of devices and one chip for each substrate preparation method, we therefore cannot assign the broader Q_i distribution uniquely to the R31 reconstruction. The larger laterally correlated structural domains observed on R31-Al_2O_3 may additionally reduce spatial averaging of local loss centers, but testing this interpretation would require correlating individual resonator locations with local morphology [51].

Regardless of this variation, both TiN films are capable of supporting resonators with similarly high Q_i values. When taken together, we can conclude that thermal reconstruction of the Al_2O_3 substrate is a viable method of substrate preparation for superconducting devices with comparable quality to those grown on substrates which were prepared chemically. Indeed, this resilience of TiN resonator performance despite the differences in substrate preparation is broadly consistent with prior literature suggesting that dielectric losses within a superconducting quantum device are mostly dominated by metal-vacuum interfaces, which changes in the interface between the substrate and the film having minimal effect on device performance [52–54].

5. Conclusion

In summary, we have demonstrated that thermally reconstructed sapphire is capable of producing highly crystalline, epitaxial films grown by MBE that have greater crystallinity than those grown on sapphire substrates prepared by aggressive chemical cleaning. We attribute this to the formation of an atomically-smooth terrace structure inherent to the R31 reconstruction that has been extensively studied and found to aid in the growth of epitaxial thin films with enhanced microstructure [19–21]. While TiN films grown on thermally reconstructed sapphire exhibited lower mosaicity and greater long-range order, these films possessed similar superconducting properties to those grown on chemically prepared substrates. It may be possible that any deviations observed in the superconducting properties of our films compared to literature, may be due to the high temperature epitaxy of these TiN thin films on sapphire substrates, potentially leading to the formation of N vacancies. The quality of this high temperature epitaxial growth may be improved further via the use of Ammonia (NH_3) as a reactive atmosphere, potentially enhancing crystallinity further while minimizing the formation of vacancies [24]. When fabricated into superconducting CPW resonators, both substrate preparation methods produce resonators with quality factors over 10^6 at single photon values, with some exceeding 10^7 at high photon numbers. No significant or systematic differences were observed in the superconducting properties or behavior of the resonators on either chip. This implies that thermal reconstruction of sapphire substrates via direct laser heating is a viable method of *in − situ* substrate preparation that by-passes aggressive chemical cleaning. Thermal reconstruction of the substrate promotes greater crystalline coherence of the epitaxially grown film while preserving the electrical properties of the deposited material. This may also present exciting opportunities for the *in − situ* growth of quantum devices and high-quality 2D materials on oxide substrates [29]. When taken together, these results establish thermally reconstructed sapphire as a robust *in-situ* platform for the epitaxial growth of superconducting nitrides, opening new avenues for the fabrication of quantum devices and other heterostructures.

Acknowledgments

All chemical preparation and fabrication steps detailed within this work were performed within the Helmholtz Nano Facility, to which we are grateful to all the technical staff [55]. We wish to specifically highlight the technical support of Jéferson R. Guimarães, Christoph Krause and Anja Zaß. The authors thank Marc Scheffler, Yayi Lin, Christine Falter and Nils von den Driesch for many insightful scientific discussions. The authors thank Lucas Bothe for assistance with RHEED operation and Amin Karimi for establishing the STM experimental setup and for his assistance with the STM measurements. The authors gratefully acknowledge support by the German Federal Ministry of Research, Technology and Space (BMFTR), funding program 'Quantum technologies—from basic research to market', project QSolid (Grant No. 13N16149) and from the European Union Flagship on Quantum Technology (OpenSuperQplus100, No. 101113946).

Data availability statement

The data that support the findings of this study are openly available at the following URL/DOI: https://doi.org/10.5281/zenodo.21263545 [56].

Conflict of interest

The authors declare no competing interests.

Author contributions

Thomas J Smart 0000-0001-8245-7677
Conceptualization (lead), Data curation (equal), Formal analysis (equal), Investigation (lead), Methodology (equal), Software (supporting), Validation (equal), Visualization (lead), Writing – original draft (lead), Writing – review & editing (equal)

Marc Neis 0000-0003-2774-4045
Conceptualization (equal), Data curation (equal), Formal analysis (equal), Investigation (equal), Methodology (equal), Software (lead), Validation (equal), Visualization (equal), Writing – original draft (supporting), Writing – review & editing (equal)

Janine Lorenz
Data curation (equal), Formal analysis (equal), Investigation (supporting), Methodology (equal), Validation (equal), Visualization (equal), Writing – original draft (supporting), Writing – review & editing (equal)

Marcello P Guardascione
Data curation (supporting), Investigation (equal), Methodology (equal), Validation (supporting)

Roudy Hanna
Data curation (supporting), Investigation (supporting), Methodology (equal), Validation (supporting)

Michael Schleenvoigt
Investigation (equal), Methodology (equal), Writing – review & editing (supporting)

Yuan Gao
Methodology (supporting), Software (supporting), Validation (supporting)

Joscha Domnick
Investigation (equal), Methodology (equal)

Benjamin Bennemann
Methodology (equal)

Abdur Rehman Jalil 0000-0003-1869-2466
Formal analysis (equal)

Jin Hee Bae
Data curation (equal)

Harsh Bhardwaj
Methodology (supporting), Software (supporting)

F Stefan Tautz 0000-0003-3583-2379
Funding acquisition (equal), Supervision (equal)

Felix Lüpke 0000-0002-6430-9627
Investigation (supporting), Methodology (supporting), Supervision (equal)

Detlev Grützmacher
Conceptualization (equal), Funding acquisition (equal), Supervision (equal)

Rami Barends
Funding acquisition (equal), Project administration (equal), Supervision (equal), Writing – original draft (equal), Writing – review & editing (equal)

Pavel A Bushev
Conceptualization (equal), Funding acquisition (equal), Project administration (equal), Supervision (equal), Writing – original draft (equal), Writing – review & editing (equal)

Peter Schüffelgen 0000-0001-7977-7848
Conceptualization (equal), Funding acquisition (equal), Supervision (equal), Writing – review & editing (equal)

Appendix A. Reflection high-energy electron diffraction (RHEED) images of R31-Al_2O_3

As described in the main text, 10×10 mm c-plane α-Al_2O_3 substrates were heated at a rate of 3 °C s^{-1} to 1700 °C, where they were held at this temperature for 200 s before being cooled back to room temperature at a rate of 3 °C s^{-1}. During heating, the thermal laser epitaxy (TLE) chamber pressure remained in the order of 10^{-9} mbar. These substrates were stored in air for six months after reconstruction. In order to verify the presence of a specific double-step $(\sqrt{31} \times \sqrt{31})\,R{\pm}9°$ (R31) surface reconstruction, RHEED was performed on the samples at 15 keV. Before imaging, the samples were baked in a ultra-high vacuum (UHV) atmosphere at 400 °C for 30 min to remove any volatile absorbates (e.g. water vapor) resulting from extended storage in air. This recovers the original surface reconstruction, which in the case of R31-Al_2O_3 is stable in air [20].

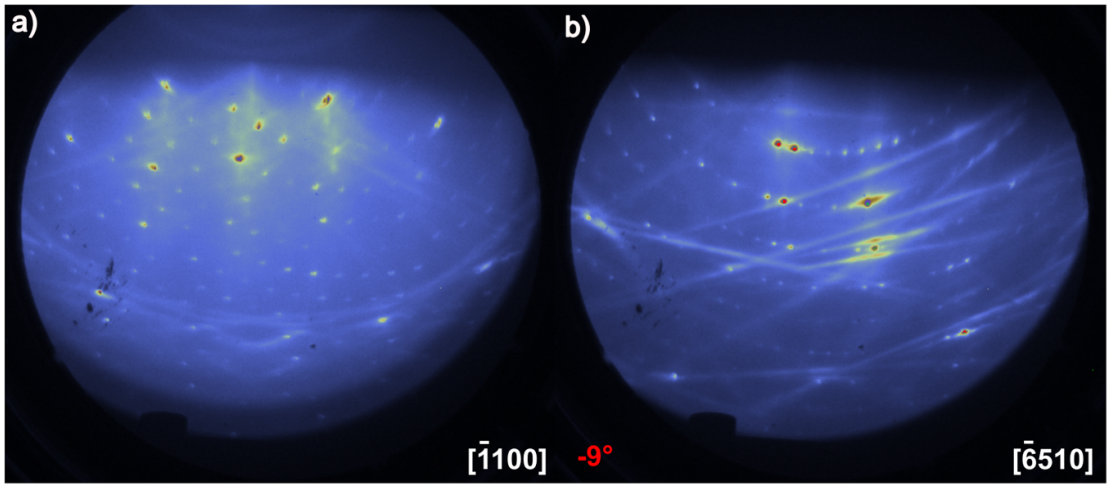


Figure A1. RHEED images of the reconstructed sapphire surface produced after being heated to 1700 °C for 200 s in UHV conditions. Prior to imaging, these substrates were stored in air for six months. The sample was baked in a UHV atmosphere at 400 °C for 30 min prior to imaging in order to remove any volatile absorbates resulting from extended storage in air. Images were taken along the [$\bar{1}$100] direction, shown in (a) and the [$\bar{6}$510] direction, taken by rotating the sample by 9° anti-clockwise (while viewing the substrate from the top). This image is shown in (b) Both of these images are consistent with prior literature of the double-step $(\sqrt{31} \times \sqrt{31})\,R{\pm}9°$ surface reconstruction [20].

As shown in figure A1, both images present sharp and well-resolved spots, implying a highly ordered 2D surface, consistent with prior literature of the reconstructed R31 surface [20, 57]. Within figure A1, all spots appear to lie upon observable Laue circles centered on the upper-right corner of the image. By rotating the pattern by −9°, corresponding to an anti-clockwise rotation, as viewed from above the substrate, the concentric circular pattern in figure A1(b) is observed. Crucially, this pattern in figure A1(b) is not present when the sample is rotated by +9°, indicating that the degeneracy of the $(\sqrt{31} \times \sqrt{31})\,R{\pm}9°$ reconstruction has been lifted, supporting a double-step R31 surface reconstruction with a singular orientation of +9°. The observation that the RHEED pattern observed in figure A1 was recovered, despite storage in air for six months supports prior literature stating that the R31 reconstruction remains stable in air and does not degrade [20]. When taken as a whole, these images confirm the presence of a stable R31 reconstruction after direct laser heating of the Al_2O_3 substrates at 1700 °C for 200 s. The lack of degeneracy in the RHEED pattern when rotating the RHEED pattern to ±9° from the [$\bar{1}$100] azimuth supports the formation of a double-step surface with a singular surface rotation of +9°, consistent with the AFM image of the same R31-Al_2O_3 surface shown in figure 1.

Appendix B. TiN/Al_2O_3 XRD pole measurements

To confirm the presence of a fixed epitaxial relation between the c-plane α-Al_2O_3 and the TiN (111) films grown on top of them, XRD pole measurements centered on TiN(111) and off-axis $Al_2O_3(10\bar{1}4)$ reflection for both the B-Al_2O_3 and R31-Al_2O_3 substrates were performed.

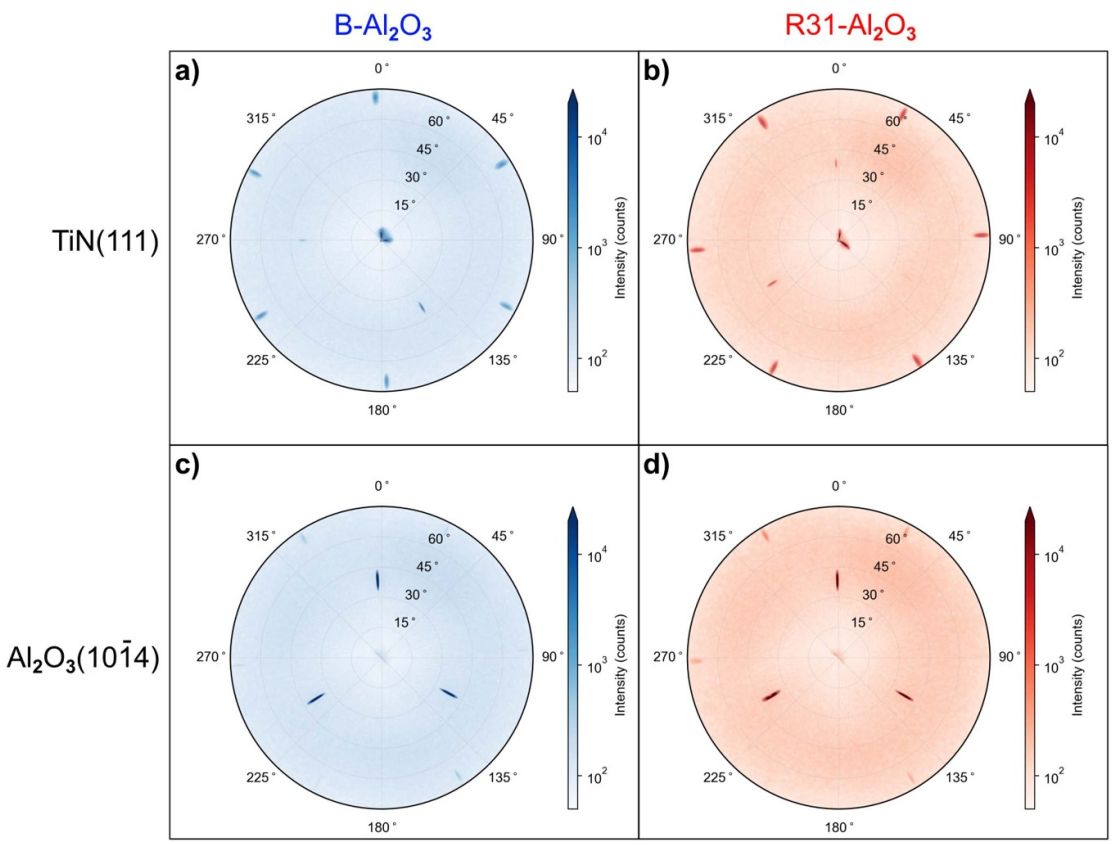


Figure B2. XRD pole figures centered around the TiN(111) and off-axis Al_2O_3 (10–14) peaks, for TiN films on R31-Al_2O_3 and B-Al_2O_3.

Pole-figure measurements shown in figure B2 reveal TiN grows epitaxially with TiN (111) ‖ $Al_2O_3(0001)$. The TiN 111 pole figures indicate six discrete off-axis poles at $\chi \sim 70.5°$, consistent with two 60°-related in-plane rotational variants. Both the reconstructed and unreconstructed sapphire substrates yield TiN (111) films with the same epitaxial orientation relationship relative to the underlying Al_2O_3 lattice. Although the absolute azimuthal positions of the pole sets differ by approximately 30° between samples, the TiN and Al_2O_3 poles rotate together, leaving their relative azimuthal relationship unchanged.

Appendix C. Superconducting properties of TiN films

Before cooling down the TiN films on B-Al_2O_3 and R31-Al_2O_3, room temperature four-point probe measurements were performed using a needle probe station to determine the resistivity, ρ of the samples. These values were determined to be 21.1 $\mu\Omega \cdot$ cm and 19.8 $\mu\Omega \cdot$ cm for TiN on B-Al_2O_3 and R31-Al_2O_3 respectively.

These samples were then placed within a dilution refrigerator with ρ being measured as a function of temperature. From the results in figure C3, the T_c of each TiN film was determined to be 5.08 K and 5.11 K on B-Al_2O_3 and R31-Al_2O_3 respectively. The value of T_c was determined as the temperature at which the superconducting transition was complete when the samples were cooled from their normal state to the superconducting state. Due to the limited resolution of the T_c measurement, it is challenging to assign a width, ΔT_c to the superconducting transition of both films. An extreme, approximate value of ΔT_c can be assigned to both films accounting for the region over which the entire superconducting

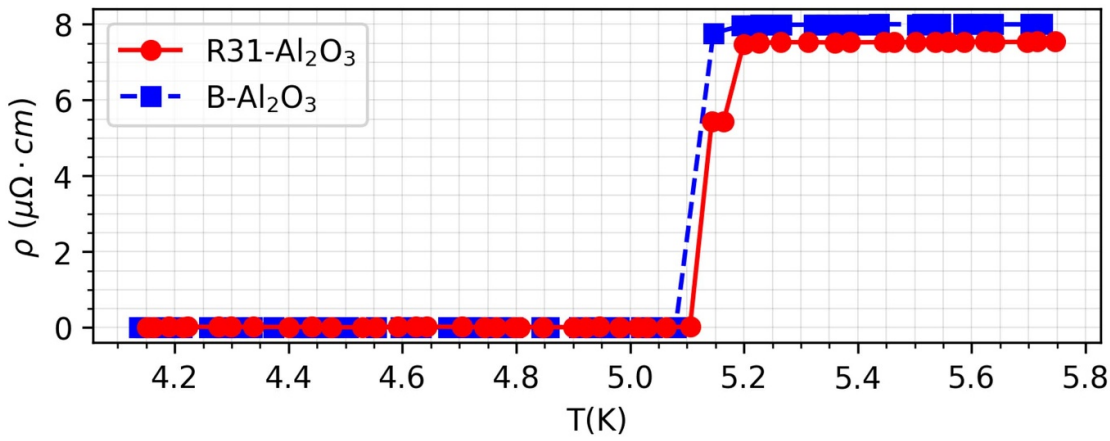


Figure C3. $\rho(T)$ around the region of T_c for $d = 106$ nm thick TiN films grown on B-Al_2O_3 and R31-Al_2O_3 substrates.

transition occurs. This results in $\Delta T_c = 0.07$ K and $\Delta T_c = 0.09$ K for TiN on B-Al_2O_3 and R31-Al_2O_3 respectively.

Appendix D. STM topography

Figure D4 depicts representative STM topographs of both samples. We attribute differences in the height variations between the STM and AFM data to the AFM having a blunter tip and thus lower lateral resolution, which leads to an underestimation of the surface roughness.

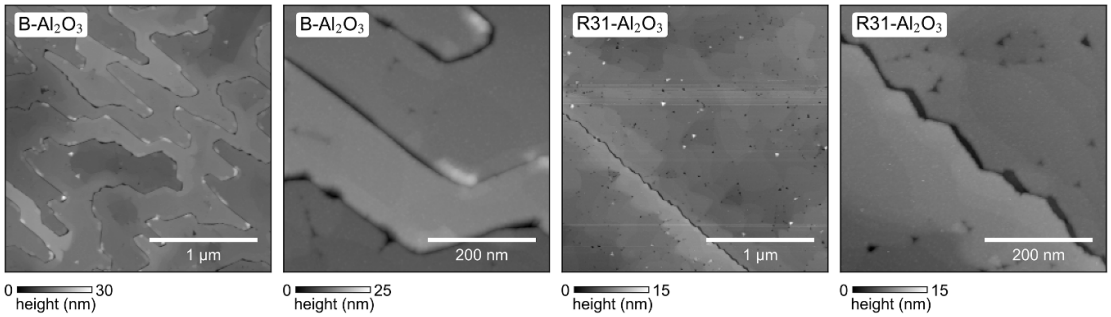


Figure D4. STM topographs of $d = 106$ nm thick TiN films grown on chemically cleaned (B-Al_2O_3) and thermally reconstructed (R31-Al_2O_3) sapphire substrates (current setpoint: 30 pA, bias voltage: 800 mV).

Appendix E. Resonator parameters

Tables 1 and 2 show the resonator parameters for all TiN resonators prepared on both R31-Al_2O_3 and B-Al_2O_3 respectively. For each resonator, both the internal quality factor, Q_i and coupling quality factor, Q_c were measured at low microwave powers, with the corresponding value of $\langle n \rangle$ indicated. All resonators possessed a coupler length of $l = 50$ μm. The raw Q_i data as a function of $\langle n \rangle$ of all measured resonators on each chip, along with the extracted median Q_i and confidence interval of each chip are shown in figure E5.

Example S_{21} fits In figures E6 and E7, raw S_{21} data measured at single photon levels from a given TiN CPW resonator are shown. Data from resonators on R31-Al_2O_3 and B-Al_2O_3 are included. To extract the properties in question a Lorentzian fit for the normalized inverse transmission $\tilde{S}_{21}^{-1}$ was used [58]:

$$\tilde{S}_{21}^{-1} = 1 + \frac{Q_i}{Q_c^*} e^{i\phi} \frac{1}{1 + 2iQ_i\delta x}. \tag{E1}$$

Table 1. Resonator parameters for $d = 106$ nm TiN film on R31-Al_2O_3 at given photon number $\langle n \rangle$.

Frequency (GHz)	Microwave power (dBm)	$\langle n \rangle$	Q_i ($\times 10^6$)	Q_c ($\times 10^6$)	s (μm)	w (μm)
4.818	−155	1.63	1.581	0.367	2	3
5.777	−150	1.28	1.149	0.106	6	10
5.872	−155	0.71	1.582	0.207	2	3
6.797	−150	0.76	1.156	0.085	6	10
6.890	−150	1.11	0.618	0.185	8	12
6.941	−145	1.35	0.218	0.626	2	3
7.846	−150	0.89	1.123	0.146	6	10
7.946	−150	0.96	1.125	0.167	8	12
8.083	−150	0.38	0.383	0.222	2	3

Table 2. Resonator parameters for $d = 106$ nm TiN film on B-Al_2O_3 at given photon number $\langle n \rangle$.

Frequency (GHz)	Microwave power (dBm)	$\langle n \rangle$	Q_i ($\times 10^6$)	Q_c ($\times 10^6$)	s (μm)	w (μm)
4.960	−155	1.21	1.826	0.254	8	12
5.340	−155	0.71	0.593	1.143	2	3
5.762	−150	1.24	1.216	0.101	6	10
5.863	−150	2.52	1.953	0.207	8	12
5.971	−135	138.41	1.630	0.617	2	3
6.827	−150	0.76	1.254	0.083	6	10
6.908	−155	0.57	1.512	0.243	2	3
7.845	−150	0.65	1.344	0.096	6	10
7.938	−150	0.96	1.198	0.164	8	12

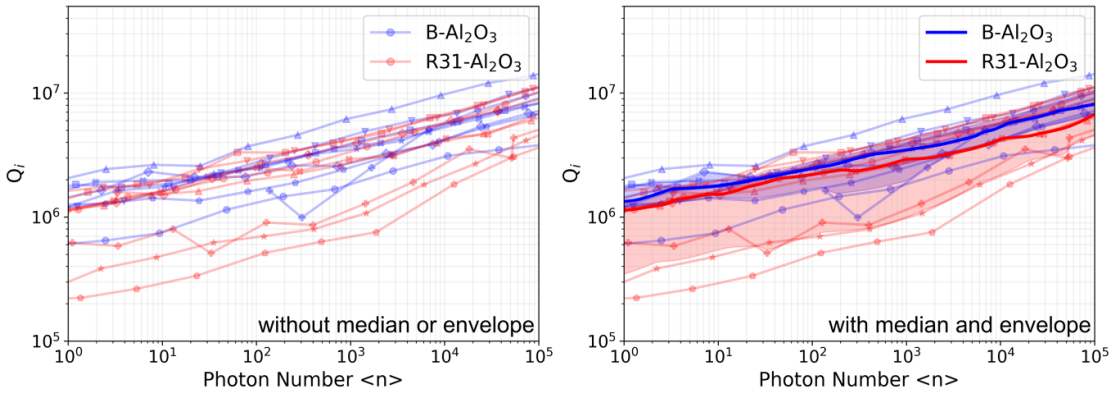


Figure E5. The first panel shows the Q_i data for all CPW resonators fabricated from $d = 106$ nm TiN films on R31-Al_2O_3 and B-Al_2O_3 respectively. Each resonator is shown with a different marker and is colored according to which chip they belong to. The second panel includes the raw data overlaid with a median Q_i value for each chip. A confidence interval is also shown for each chip. This confidence interval corresponds to one standard deviation from the mean Q_i value.

With the internal quality factor, Q_i, the rescaled coupling quality factor $Q_c^* = (Z_0/|Z|)$, impedance mismatch ϕ, and the linear frequency detuning from the resonance frequency $\delta x = (f - f_0)/f_0$. Additionally the resonator is corrected for various external electrical factors. The average photon number of the resonators $\langle n \rangle$ was calculated via [59]:

$$\langle n \rangle = \frac{4}{\pi h f_r} \cdot C P_{in} Z_{in} \frac{Q_l^2}{Q_c}. \tag{E2}$$

Using the total resonator capacitance, C, feedline power, P_{in}, feedline impedance Z_{in} and the loaded quality factor $Q_l = \frac{Q_i Q_c}{Q_i + Q_c}$.

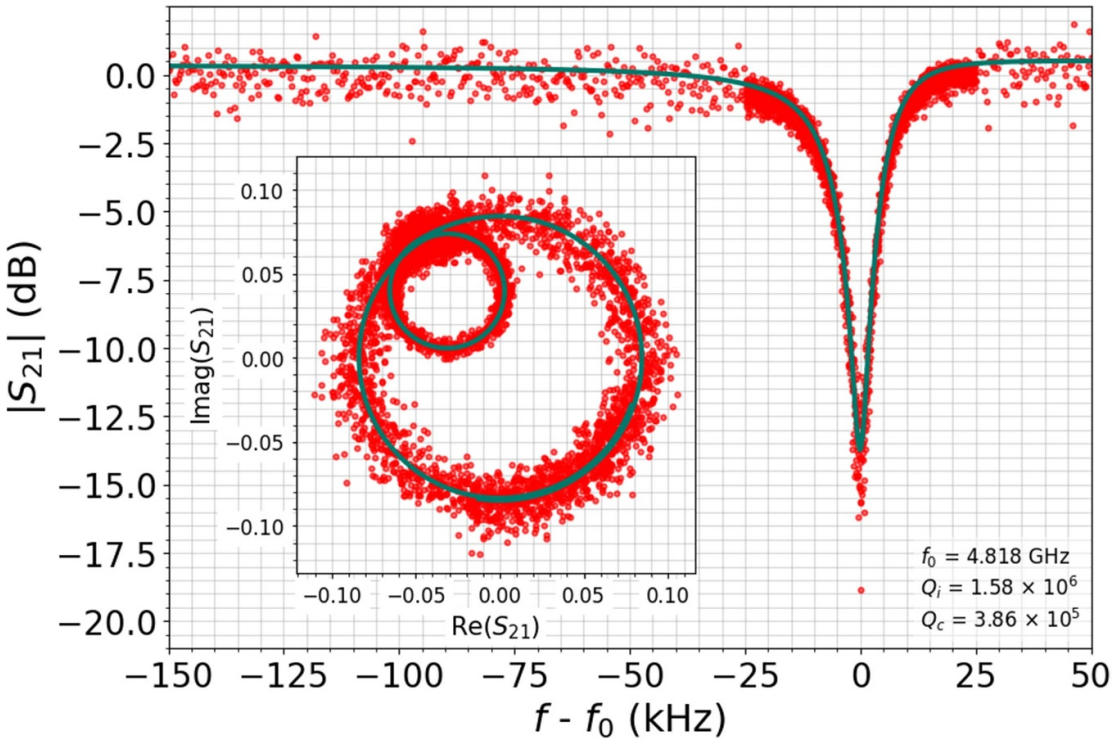


Figure E6. S_{21} as a function of frequency, f for a TiN resonator on R31-Al_2O_3 with a resonant frequency, $f_0 = 4.818$ GHz. All data was taken at $T \sim 20$ mK and measured at a microwave power of −155 dBm corresponding to $\langle n \rangle \sim 1.68$.

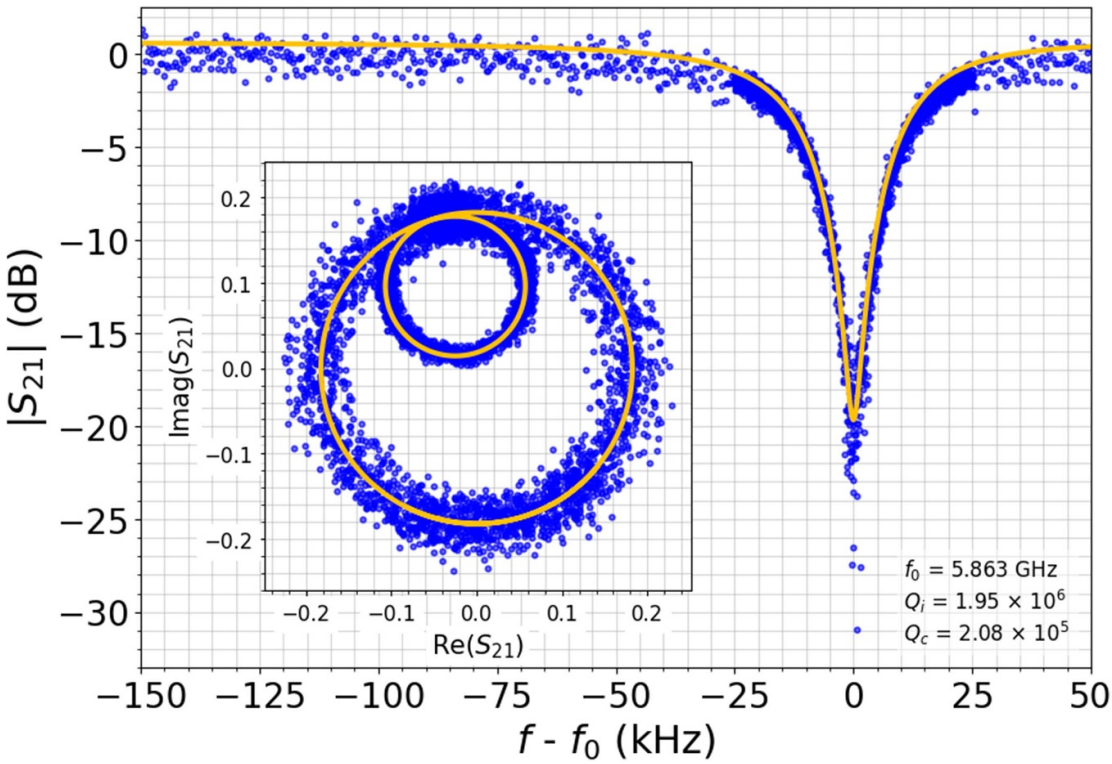


Figure E7. S_{21} as a function of frequency, f for a TiN resonator on B-Al_2O_3 with a resonant frequency, $f_0 = 5.863$ GHz. All data was taken at $T \sim 25$ mK and measured at a microwave power of −150 dBm corresponding to $\langle n \rangle \sim 2.52$.

References

[1] Kuroda K and Yuda M 1988 Niobium-stress influence on Nb/Al-oxide/Nb josephson junctions *J. Appl. Phys.* **63** 2352
[2] Barends R *et al* 2014 Superconducting quantum circuits at the surface code threshold for fault tolerance *Nature* **508** 500
[3] Nakamura Y, Pashkin Y A and Tsai J S 1999 Coherent control of macroscopic quantum states in a single-cooper-pair box *Nature* **398** 786
[4] Wang Z, Kawakami A, Uzawa Y and Komiyama B 1994 High critical current density NbN/AlN/NbN tunnel junctions fabricated on ambient temperature MgO substrates *Appl. Phys. Lett.* **64** 2034
[5] Face D W and Prober D E 1987 Fabrication and dc characteristics of small-area tantalum and niobium superconducting tunnel junctions *J. Appl. Phys.* **62** 3257
[6] Place A P M *et al* 2021 New material platform for superconducting transmon qubits with coherence times exceeding 0.3 milliseconds *Nat. Commun.* **12** 1779
[7] Sundgren J-E 1985 Structure and properties of TiN coatings *Thin Solid Films* **128** 21
[8] Lengauer W 2015 Nitrides: Transition metal solid-state chemistry *Encyclopedia of Inorganic and Bioinorganic Chemistry* (Wiley) pp 1–24
[9] Mauersberger T, Trommer J, Sharma S, Knaut M, Pohl D, Rellinghaus B, Mikolajick T and Heinzig A 2021 Single-step reactive ion etching process for device integration of hafnium-zirconium-oxide (HZO)/titanium nitride (TiN) stacks *Semicond. Sci. Technol.* **36** 095025
[10] Briggs J A, Naik G V, Petach T A, Baum B K, Goldhaber-Gordon D and Dionne J A 2016 Fully CMOS-compatible titanium nitride nanoantennas *Appl. Phys. Lett.* **108** 051110
[11] Wright J *et al* 2021 Unexplored MBE growth mode reveals new properties of superconducting NbN *Phys. Rev. Mater.* **5** 024802
[12] Takiguchi K, Krockenberger Y, Ichibha T, Hongo K, Maezono R, Taniyasu Y and Yamamoto H 2025 Electronic transport properties of titanium nitride grown by molecular beam epitaxy *Phys. Rev. B* **112** 224520
[13] Richardson C J K, Alexander A, Weddle C G, Arey B and Olszta M 2020 Low-loss superconducting titanium nitride grown using plasma-assisted molecular beam epitaxy *J. Appl. Phys.* **127** 235302
[14] Vissers M R, Gao J, Wisbey D S, Hite D A, Tsuei C C, Corcoles A D, Steffen M and Pappas D P 2010 Low loss superconducting titanium nitride coplanar waveguide resonators *Appl. Phys. Lett.* **97** 232509
[15] Ohya S *et al* 2013 Room temperature deposition of sputtered TiN films for superconducting coplanar waveguide resonators *Supercond. Sci. Technol.* **27** 015009
[16] Shearrow A, Koolstra G, Whiteley S J, Earnest N, Barry P S, Heremans F J, Awschalom D D, Shirokoff E and Schuster D I 2018 Atomic layer deposition of titanium nitride for quantum circuits *Appl. Phys. Lett.* **113** 212601
[17] Zhang D, Wang Y and Gan Y 2013 Characterization of critically cleaned sapphire single-crystal substrates by atomic force microscopy, XPS and contact angle measurements *Appl. Surf. Sci.* **274** 405
[18] Braun W, Jäger M, Laskin G, Ngabonziza P, Voesch W, Wittlich P and Mannhart J 2020 In situ thermal preparation of oxide surfaces *APL Mater.* **8** 071112
[19] Smart T J, Kim D Y and Braun W 2024 Twin-free thermal laser epitaxy of Si on sapphire *J. Vac. Sci. Technol. B* **42** 062204
[20] Smink S, Majer L N, Boschker H, Mannhart J and Braun W 2024 Long-range atomic order on double-stepped Al_2O_3(0001) surfaces *Adv. Mater.* **36** 2312899
[21] Majer L N, Smink S, Braun W, Fenk B, Harbola V, Stuhlhofer B, Wang H, van Aken P A, Mannhart J and Hensling F V E 2024 α-Ta films on c-plane sapphire with enhanced microstructure *APL Mater.* **12** 091108
[22] Majer L N, Smink S, Braun W, Wang H, van Aken P A, Mannhart J and Hensling F V E 2024 Growth of high-quality ruthenium films on sapphire *J. Vac. Sci. Technol. A* **42** 052702
[23] Kim D Y, Smart T J, Mannhart J and Braun W 2023 Thermal laser epitaxy of carbon films *Cryst. Growth Des.* **23** 8087
[24] Kim D Y *et al* 2025 Nitride thin films grown by thermal laser epitaxy *APL Mater.* **13** 011125
[25] Brucker M, Harbola V, Mannhart J, Smink S, Whittles T J and Hensling F V 2025 Morphology of various single faced sapphire surfaces prepared by rapid thermal annealing *Appl. Surf. Sci.* **696** 162929
[26] Braun W and Mannhart J 2019 Film deposition by thermal laser evaporation *AIP Adv.* **9** 085310
[27] Smart T J 2023 Thermal laser epitaxy : from fundamental physics to the growth of novel thin films *PhD Thesis* University of Stuttgart (available at: https://dx.doi.org/10.18419/opus-13081)
[28] Smart T J, Mannhart J and Braun W 2021 Thermal laser evaporation of elements from across the periodic table *J. Laser Appl.* **33** 02205
[29] Hanna R *et al* 2026 On-chip stencil lithography for superconducting qubits *Appl. Phys. Rev.* **13** 021403
[30] Hütner-Reisch J I, Conti A, Kugler D, Mittendorfer F, Schmid M, Diebold U and Balajka J 2026 Afm imaging reveals the unreconstructed α-Al_2O_3(0001) surface to be inhomogeneous and rough *Nat. Commun.* **17** 4692
[31] Rasic D, Sachan R, Chisholm M F, Prater J and Narayan J 2017 Room temperature growth of epitaxial titanium nitride films by pulsed laser deposition *Cryst. Growth Des.* **17** 6634
[32] Narayan J and Larson B C 2003 Domain epitaxy: a unified paradigm for thin film growth *J. Appl. Phys.* **93** 278
[33] Catellani A and Calzolari A 2017 Plasmonic properties of refractory titanium nitride *Phys. Rev. B* **95** 115145
[34] Zhang R *et al* 2021 Crystal orientation-dependent oxidation of epitaxial TiN films with tunable plasmonics *ACS Photon.* **8** 847
[35] Moram M A and Vickers M E 2009 x-ray diffraction of III-nitrides *Rep. Prog. Phys.* **72** 036502
[36] Calamba K M, Pierson J F, Bruyére S, Febvrier A L, Eklund P, Barrirero J, Mücklich F, Boyd R, Johansson Jõesaar M P and Odén M 2019 Dislocation structure and microstrain evolution during spinodal decomposition of reactive magnetron sputtered heteroepitatial c-$(Ti_{0.37},Al_{0.63})N$/c-TiN films grown on MgO(001) and (111) substrates *J. Appl. Phys.* **125** 105301
[37] Kamlapure A, Das T, Ganguli S C, Parmar J B, Bhattacharyya S and Raychaudhuri P 2013 Emergence of nanoscale inhomogeneity in the superconducting state of a homogeneously disordered conventional superconductor *Sci. Rep.* **3** 2979
[38] Dynes R C, White A E, Graybeal J M and Garno J P 1986 Breakdown of eliashberg theory for two-dimensional superconductivity in the presence of disorder *Phys. Rev. Lett.* **57** 2195
[39] Liao W-T, Kohler T P, Osborn K D, Butera R E, Lobb C J, Wellstood F C and Dreyer M 2019 Scanning tunneling andreev microscopy of titanium nitride thin films *Phys. Rev. B* **100** 214505
[40] Tinkham M 1996 *Introduction to Superconductivity* (McGraw-Hill Inc.)

[41] Gao R, Yu W, Deng H, Ku H-S, Li Z, Wang M, Miao X, Lin Y and Deng C 2022 Epitaxial titanium nitride microwave resonators: Structural, chemical, electrical and microwave properties *Phys. Rev. Mater.* **6** 036202
[42] Probst S, Song F B, Bushev P A, Ustinov A V and Weides M 2015 Efficient and robust analysis of complex scattering data under noise in microwave resonators *Rev. Sci. Instrum.* **86** 024706
[43] Khalil M S, Stoutimore M J A, Wellstood F C and Osborn K D 2012 An analysis method for asymmetric resonator transmission applied to superconducting devices *J. Appl. Phys.* **111** 054510
[44] Leduc H G *et al* 2010 Titanium nitride films for ultrasensitive microresonator detectors *Appl. Phys. Lett.* **97** 102509
[45] Fu J-H *et al* 2023 Oriented lateral growth of two-dimensional materials on c-plane sapphire *Nat. Nanotechnol.* **18** 1289
[46] Zhang T *et al* 2025 Increasing the superconductivity of tin epitaxial films by lattice strain toward a record critical temperature *Phys. Rev. B* **112** 045403
[47] Schulberg M T, Allendorf M D and Outka D A 1996 Aspects of nitrogen surface chemistry relevant to TiN chemical vapor deposition *J. Vac. Sci. Technol. A* **14** 3228–35
[48] Melville A *et al* 2020 Comparison of dielectric loss in titanium nitride and aluminum superconducting resonators *Appl. Phys. Lett.* **117** 124004
[49] Calusine G *et al* 2018 Analysis and mitigation of interface losses in trenched superconducting coplanar waveguide resonators *Appl. Phys. Lett.* **112** 062601
[50] Lang S *et al* 2026 Optimizing CMOS-compatible, superconducting titanium nitride resonators: Deposition conditions and structuring processes *Appl. Phys. Rev.* **13** 031403
[51] Chen C, Aghaeimeibodi S, Sato Y, Matheny M H, Painter O and Gao J 2026 Broadband high-precision measurement of two-level-system loss using multiwavelength superconducting resonators *Phys. Rev. Appl.* **25** 014045
[52] Woods W, Calusine G, Melville A, Sevi A, Golden E, Kim D, Rosenberg D, Yoder J and Oliver W 2019 Determining interface dielectric losses in superconducting coplanar-waveguide resonators *Phys. Rev. Appl.* **12** 014012
[53] Altoé M V P *et al* 2022 Localization and mitigation of loss in niobium superconducting circuits *PRX Quantum* **3** 020312
[54] Murthy A A *et al* 2025 Identifying materials-level sources of performance variation in superconducting transmon qubits (arXiv:2503.14424)
[55] Albrecht W, Moers J and Hermanns B 2017 HNF - Helmholtz nano facility *J. Large-Scale Res. Facil.* **3** A112
[56] Smart T J*et al* 2026 Data for results of "Highly crystalline superconducting TiN resonators grown on thermally reconstructed sapphire *Zenodo* (available at: https://doi.org/10.5281/zenodo.21263545)
[57] Tosaka A, Kitamura T, Sugiyama T, Koyama K and Shigeta Y 2014 Influence of step morphology on the structural phase transition of the α-al$_2$o$_3$(0001) surface *Appl. Phys. Lett.* **104** 221601
[58] Megrant A *et al* 2012 Planar superconducting resonators with internal quality factors above one million *Appl. Phys. Lett.* **100** 113510
[59] Barends R 2009 Photon-detecting superconducting resonators *Dissertation (TU Delft)* Delft University of Technology